

Supplementary Information for

Sequential localization of a complex electron fluid

Valentina Martelli, Ang Cai, Emilian M Nica, Mathieu Taupin, Andrey Prokofiev, Chia-Chuan Liu, Hsin-Hua Lai, Rong Yu, Kevin Ingersent, Robert K uchler, Andre M. Strydom, Diana Geiger, Jonathan Haenel, Julio Larrea, Qimiao Si, Silke Paschen

Silke Paschen or Qimiao Si.

E-mail: paschen@ifp.tuwien.ac.at or qmsi@rice.edu

This PDF file includes:

Figs. S1 to S8

References for SI reference citations

Section S1. Synthesis

The polycrystalline starting material for the crystal growth was prepared from high-purity elements (Ce 99.99%, Pd 99.998%, Si 99.9999%) by radio-frequency heating in a horizontal copper boat. The crystal growth was performed by a variant of the floating-zone melting technique in a 4-mirror furnace (Crystal Systems Cooperation) under Ar 6.0 protective atmosphere, as reported previously (protocol for the single crystal “sc1”) (1). Due to a finite homogeneity range, there is a slight compositional gradient along the growth direction, which makes small stoichiometry differences between different sample pieces unavoidable. Different samples then have slightly different residual resistance ratios (between 3 and 6 for “sc1”) and quantum critical fields. The sample used for thermal expansion and magnetostriction is very similar to the sample studied by Ono et al. (2), as seen from the excellent agreement of the phase boundaries in Fig. 1(b). The samples used for our transport and specific heat measurements had slightly lower critical fields. This is why we slightly rescaled the field scale of Fig. 1(b) to match the contour plot in Fig. 2(a), and why the quantum critical behavior in Fig. 2(c) occurs for slightly lower fields in specific heat than in thermal expansion.

Section S2. Characterization

The magnetotransport measurements were performed by a standard 4-point ac technique in an Oxford dilution refrigerator, using spot-welded Au contacts and low-temperature transformers. We chose to study the phase diagram with magnetic field applied along the crystallographic [001] direction because this makes the crossover region associated with the quantum critical point (QCP) at B_Q observable within the available field range; for fields along [110] and [111], B_Q is much larger (Refs. 2, 3) and this would not be the case. Nevertheless, we expect qualitatively similar behavior for all field directions. Specific heat was measured using a relaxation-type technique in a dilution refrigerator from Quantum Design. Magnetostriction and thermal expansion were measured using a high-resolution capacitance dilatometer in an Oxford dilution refrigerator.

Section S3. Experimental data analysis

The contour plot in Fig. 2(a) was obtained by fitting temperature-dependent electrical resistivity curves at fixed magnetic fields in overlapping temperature ranges to $\rho = \rho_0 + A' \cdot T^a$, taking the logarithmic derivative of $\rho - \rho_0$ with respect to temperature, and interpolating between the obtained a values.

The crossover in the magnetoresistance at B^* (Fig. 3(b),(c)) was fitted with the empirical crossover function

$$\rho(B) = A_2 - \frac{A_2 - A_1}{1 + (B/B^*)^p} \quad [2]$$

introduced in Ref. 4. The crossover in the Hall resistivity (Fig. 3(d)-(f)) was modeled with the integral over these fitting functions. As shown in Fig. 3(a),(d),(e), background contributions are superimposed on these crossovers and have to be subtracted prior to the analysis. In case of the magnetoresistance, the background is well captured by a simple linear-in-field contribution (Fig. 3(a)). For the Hall resistivity we use data taken on another single crystal from the same batch, with field applied along [111]. As for this field direction there is no QCP in the field range around 2 T of interest to us here (2, 3), this subtraction reveals the contribution due to the QCP at B_Q . The FWHM is obtained graphically from the fit curves.

The anomalous Hall effect of $\text{Ce}_3\text{Pd}_{20}\text{Si}_6$ was shown to be negligible at low temperatures, both in the linear response regime and at the QCP at B_N (Ref. 5). Here we show that this is also true for the QCP at B_Q . We estimate the anomalous contribution to the Hall resistivity due to skew scattering (6)

$$\rho_H^a = \gamma \rho_{\text{skew}} \mu_0 M \quad [3]$$

from published magnetization data (3) for M , the magnetoresistance for fields either along [001] or along [111] for ρ_{skew} , and the coefficient $\gamma = 1.29 \text{ m}^2/\text{Vs}$ determined previously (5). To bring the resulting ρ_H^a to the same scale and sign as the measured Hall resistivity, we have to rescale γ by -0.36 (fig. S4). The $\rho_H^a(B)$ curves obtained with $\rho(B|[001])$ and $\rho(B|[111])$ are very similar, showing that the step-like feature is due to $M(B)$. Importantly, both $\rho_H^a(B)$ curves share no similarity with the measured Hall resistivity that displays a kink as opposed to the step-like change of $\rho_H^a(B)$. We thus conclude that the skew scattering mechanism is also irrelevant at the QCP at B_Q , and is certainly not the origin of the observed Hall crossover.

Section S4. Local degrees of freedom

The Ce^{3+} ion in $\text{Ce}_3\text{Pd}_{20}\text{Si}_6$ has one localized $4f$ electron with total angular momentum $J = 5/2$. In a cubic environment, the crystal electric field splits this six-fold degenerate multiplet into a Γ_8 quartet and a Γ_7 doublet. The analysis of temperature dependent inelastic neutron scattering and entropy data revealed that the Γ_8 quartet is the ground state, at least for the $8c$ site (7). As this site, which forms a simple cubic sublattice with lattice parameter $a/2$, is responsible for both the AFM and the AFQ order (8), and thus also for the quantum criticality arising at the border of these phases, it is the only site of interest to us here. Whether the $4a$ site is magnetically silent due to enhanced frustration of the fcc lattice formed by this site, or due to enhanced Kondo screening at this site, remains to be clarified by future experiments, but is not pertinent to this work.

The Γ_8 quartet, that comprises three dipoles, five quadrupoles, and seven octupoles, can be described through two pseudospin operators, σ and τ , which respectively act on the Kramers and non-Kramers doublet states of the Γ_8 multiplet (9). Both dipolar (magnetic) and quadrupolar order (and likely even octupolar order) may arise via the RKKY interaction between the local multipolar moments (9). It was also shown that (π, π, π) AFQ order, which is consistent with experiments (8), has a zero net quadrupolar moment; as such it cannot directly couple to elastic distortion and thus preserves the cubic symmetry (10).

Section S5. Theoretical analysis for sequential quantum phase transitions

The multipolar Kondo lattice model corresponds to the Hamiltonian

$$H_{\text{KL}} = H_f + H_K + H_c \quad . \quad (4)$$

The first part describes the RKKY interaction among the Γ_8 local moments, and is given by $H_f = \sum_{ij} [I_{ij}^\sigma \sigma_i^z \sigma_j^z + I_{ij}^\tau \tau_i^z \tau_j^z + I_{ij}^m (\sigma_i^z \otimes \tau_i^z) (\sigma_j^z \otimes \tau_j^z)]$. Here, σ , τ , and $\sigma \otimes \tau$ express the spin and orbital operators and their tensor product, respectively. The second part specifies the Kondo coupling between the local moments and their conduction-electron counterparts and reads

$$H_K = \sum_i H_{K,i} = \sum_i J_K^\sigma \sigma_i \cdot \sigma_{i,c} + \sum_i J_K^\tau \tau_i \cdot \tau_{i,c} + \sum_i J_K^m (\sigma_i \otimes \tau_i) \cdot (\sigma_{i,c} \otimes \tau_{i,c}) \quad . \quad (5)$$

The conduction electron operators entering H_K are defined as

$$\sigma_{i,c} = \frac{1}{2} \sum_{\sigma\sigma',\tau} c_{i\sigma\tau}^\dagger \mathbf{s}_{\sigma\sigma'} c_{i\sigma'\tau} ; \quad \tau_{i,c} = \frac{1}{2} \sum_{\sigma,\tau\tau'} c_{i\sigma\tau}^\dagger \mathbf{t}_{\tau\tau'} c_{i\sigma\tau'} ; \quad \sigma_{i,c} \otimes \tau_{i,c} = \frac{1}{2} \sum_{\sigma\sigma'\tau\tau'} c_{i\sigma\tau}^\dagger \mathbf{s}_{\sigma\sigma'} \mathbf{t}_{\tau\tau'} c_{i\sigma'\tau'} \quad (6)$$

where $\mathbf{s}_{\sigma\sigma'}$ and $\mathbf{t}_{\tau\tau'}$ are Pauli matrices in the spin and orbital subspaces, respectively, and $c_{i\sigma\tau}^\dagger$ creates a conduction electron at site i with spin component σ and orbital component τ . Finally, $H_c = \sum_{\mathbf{k}\sigma\tau} \epsilon_{\mathbf{k}\sigma\tau} c_{\mathbf{k}\sigma\tau}^\dagger c_{\mathbf{k}\sigma\tau}$ defines the kinetic energy of the conduction electrons. Note that the paramagnetic Kondo-entangled fixed point will have an enhanced SU(4) symmetry. Correspondingly, we have taken both H_K and H_c to be rotationally invariant in both the spin and orbital spaces. Nonetheless, in the Γ_8 subspace, the Hamiltonian is in general anisotropic in both spaces. The Ising anisotropic coupling in H_f was used to make the calculations feasible. However, because (i) the Kondo-screened ground state has SU(4) symmetry regardless of whether the Hamiltonian is already SU(4) symmetric or contains anisotropies such as the Ising type, and (ii) the magnetic and quadrupolar orders operate regardless of whether the underlying model is SU(4), SU(2) \times SU(2), or Ising anisotropic, we expect our result of a sequential Kondo destruction to be generic.

Under extended dynamical mean field theory (11, 12), H_{KL} is studied through an impurity model with self-consistently determined fermionic and bosonic baths. This procedure leads to a multipolar Bose-Fermi Kondo model, which reads

$$H_{\text{BFK}} = H_K + H_{\text{BK}} + H_{\text{B0}} \quad . \quad (7)$$

Here, $H_K = H_{K0} + H_c$ describes the local moment at site 0 being Kondo-coupled to the conduction electrons. In addition, H_{BK} describes the Bose-Kondo coupling between the local moment and the bosonic baths; it is given by $H_{\text{BK}} = g_\sigma \sigma^z \phi_\sigma + g_\tau \tau^z \phi_\tau + g_m (\sigma^z \otimes \tau^z) \phi_m$, with $\phi_\kappa = \sum_q (\phi_{\kappa,q}^\dagger + \phi_{\kappa,-q})$ for $\kappa = \sigma, \tau, m$. The sign of g_κ is immaterial and, for definiteness, each will be chosen to be positive. Finally, H_{B0} specifies the dynamics of the bosonic baths, and is given by $H_{\text{B0}} = \sum_{\kappa=\sigma,\tau,m} \sum_q \omega_{\kappa,q} \phi_{\kappa,q}^\dagger \phi_{\kappa,q}$.

For the pure (fermionic) Kondo problem, the exactly, under- and over-screened Kondo models refer to the cases in which the number of conduction-electron channels is exactly equal to, less than, or larger than the degeneracy of the local multiplet (13). Our model corresponds to the exactly screened case, with 4 channels of conduction electrons coupled to a local quartet. When the Kondo couplings for σ , τ and m , J_K^σ , J_K^τ , and J_K^m , are equal to each other, the model has an SU(4) symmetry. When these couplings are different, the symmetry is reduced to SU(2) \times SU(2). Even when the model lacks the SU(4) symmetry, the system flows to the exactly screened (Fermi liquid) SU(4) Kondo fixed point (14, 15). This is analogous to what happens in the more familiar SU(2) case, in which models with anisotropic Kondo coupling in the SU(2) space are well known to flow towards a Kondo fixed point with a restored SU(2) symmetry (13).

The model in the presence of bosonic Kondo couplings has not been studied before. Based on the above observations, we will carry out calculations for the (fermionic) Kondo part to have an SU(4) symmetry, but treat the bosonic couplings with Ising anisotropy. For the Bose-Fermi Kondo model, it has been found that i) the Kondo-screened fixed point is (as for the pure fermionic Kondo model) the same regardless of whether the model preserves or breaks the SU(2) symmetry; ii) the phase diagram is similar between the SU(2) and broken SU(2) symmetry cases in so far as the existence of both the unstable fixed point and the Kondo-destroyed phase (16, 17) are concerned. This suggests that, in the SU(4) case we study, the overall phase diagram of the model with different kinds of symmetries in the SU(4) space is captured by the calculations with Ising-anisotropic bosonic couplings.

We study the fate of the SU(4) Kondo-entangled state of H_{BFK} using the hybridization-expansion continuous-time quantum Monte Carlo method (18, 19). This is accomplished through the multipolar Bose-Fermi Anderson model, with H_K being replaced by the hybridization of a localized two-orbital spin-1/2 f electron to the conduction electrons. We incorporate an onsite Hubbard interaction U containing both intra- and inter-orbital parts and an energy level ϵ for the f electron, and an onsite hybridization V .

In addition, σ^z is now understood as $\sigma^z = \frac{1}{2} \sum_{\sigma\sigma',\tau} f_{\sigma\tau}^\dagger s_{\sigma\sigma'}^\tau f_{\sigma'\tau}$, and likewise for τ^z and $\sigma^z \otimes \tau^z$. When U is sufficiently large, a canonical (Schrieffer-Wolff) transformation determines the Kondo couplings J_K^κ .

We construct the zero-temperature phase diagram in terms of the spin and orbital bosonic bath couplings g_σ and g_τ . We consider fixed spectra of the fermionic and bosonic baths as follows: The conduction electrons have a density of states, $\rho_c = \sum_{\mathbf{k}} \delta(\epsilon - \epsilon_{\mathbf{k}\sigma\tau}) = \rho_0 \Theta(|D - \epsilon|)$, with $\rho_0 = 1/(2D)$, whereas the bosonic bath has a sub-Ohmic spectrum, $\rho_{\text{B},\kappa}(\omega) = \sum_q \delta(\omega - \omega_{\kappa,q}) = K_0 \omega^s e^{-\omega/\Lambda} \Theta(\omega)$ with $s = 0.6$. We choose $D = 1$, set the soft energy cutoff to be $\Lambda = 1$, fix the

hybridization strength in terms of $\Gamma_0 = \pi\rho_0V^2 = 0.1$, and determine K_0 by the normalization condition $\int_0^\infty \rho_B(\omega)d\omega = 1$. The results reported here have been derived by setting $U = 1$ and $\epsilon = 0.5$. We work at quarter filling of the f electrons as is appropriate for $\text{Ce}_3\text{Pd}_{20}\text{Si}_6$.

To detect the localization to delocalization transition associated with the spin and orbital degrees of freedom, we calculate the Binder ratios U_σ and U_τ , which are defined as

$$U_\sigma = \frac{\left\langle \left(\frac{1}{\beta} \int_0^\beta \sigma^z(\tau) d\tau \right)^4 \right\rangle}{\left\langle \left(\frac{1}{\beta} \int_0^\beta \sigma^z(\tau) d\tau \right)^2 \right\rangle^2} ; \quad U_\tau = \frac{\left\langle \left(\frac{1}{\beta} \int_0^\beta \tau^z(\tau) d\tau \right)^4 \right\rangle}{\left\langle \left(\frac{1}{\beta} \int_0^\beta \tau^z(\tau) d\tau \right)^2 \right\rangle^2} . \quad [8]$$

Here, $\beta = 1/T$ is the inverse temperature, which plays the role of the effective system size. A second-order quantum phase transition is determined by the criterion that U_σ or U_τ is system size independent at the critical point (20). In other words, we can detect the QCP by examining the crossing point of U_σ and U_τ measured as a function of the control parameter at different temperatures. This is illustrated in fig. S6, where we plot the Binder ratios U_σ and U_τ obtained at various β values along the parameter cut δ of Fig. 4(b). We find that the crossing points of U_σ and U_τ are well separated; along this parameter cut δ , the former is at $g_{1c,\sigma} = 0.78$ and the latter at $g_{1c,\tau} = 0.64$.

Further evidence for the sequential localization comes from performing scaling collapses of the form

$$U_\sigma(g_1, \beta) = f(\beta^{1/\nu}(g_1 - g_{1c,\sigma}) + A/\beta^{\varphi/\nu}) \quad [9]$$

$$U_\tau(g_1, \beta) = f(\beta^{1/\nu}(g_1 - g_{1c,\tau}) + A/\beta^{\varphi/\nu}) \quad [10]$$

for U_σ and U_τ close to each QCP. Here f is a universal function, $g_{1c,\sigma}$ and $g_{1c,\tau}$ are the corresponding critical coupling for the spin (U_σ) and orbital sector (U_τ), and ν is the correlation length of the QCP. The term $A/\beta^{\varphi/\nu}$ accounts for sub-leading finite temperature corrections ($-\varphi$ is the scaling dimension of the leading irrelevant operator at the QCP). The collapsed results are shown in fig. S7. We find $g_{1c,\sigma} = 0.78$ for U_σ and $g_{1c,\tau} = 0.64$ for U_τ , in agreement with the previous estimates from the crossing points. The reciprocal correlation length exponent is found to be $\nu^{-1} = 0.51$ for both QCPs. These results establish the two consecutive transitions. The final theoretical phase diagram (Fig. 4(b)) is obtained by combining these results with those from calculations done along various additional parameter cuts.

Section S6. Dynamical Kondo effect in the multipolar Bose-Fermi Kondo model

An important feature of our experimental observation is the enhanced effective mass in the phases involving Kondo destruction (KD, Fig. 4(c)). This feature is similar to what happens in the Kondo-destroyed phase in the spin-only case, where it was attributed to a dynamical Kondo effect (21). Here we explore such an effect in the multipolar Bose-Fermi Kondo (BFK) model. The existence of both spins and orbitals, and the condition that the Γ_8 multiplet is quarter filled, make the calculations more challenging than in the $\text{SU}(2)$ and Ising-anisotropic cases of the spin-only BFK model (21). Nonetheless, the Binder cumulants show two stages of crossings (fig. S6), evidencing sequential Kondo destruction QCPs. Across each QCP, the Binder cumulants show scaling collapse (fig. S7). These properties parallel what happens across the Kondo-destruction QCP of the spin-only BFK model (21).

As in Section S5, σ^z and τ^z are the spin and orbital component of the local moment, while $\sigma_{0,c}^z$ and $\tau_{0,c}^z$ are the conduction electron counterparts at site 0. We are interested in two quantities, $\langle \sigma^z \sigma_{0,c}^z \rangle$ and $\langle \tau^z \tau_{0,c}^z \rangle$. These are the analogues of $\langle S_f^z s_c^z \rangle$ for the Ising BFK model (21), where this expectation value being nonzero was demonstrated as a diagnostic of the dynamical Kondo effect (21).

As shown in fig. S8, we follow the same trajectory as used in Fig. 4(b) and fig. S6, and calculate the evolution of $\langle \sigma^z \sigma_{0,c}^z \rangle$ and $\langle \tau^z \tau_{0,c}^z \rangle$ as a function of $g_1 = g_\sigma + g_\tau$, where g_σ and g_τ are again the coupling constant of σ^z and τ^z to their bosonic baths. The position of the two consecutive QCPs for the spin and orbital sectors are also marked on the horizontal axis. They are approximately located at $g_1 = 0.78$ for the spin sector and $g_1 = 0.64$ for the orbital sector. We see that similar to what happens in the Ising BFK model (21), here both $\langle \sigma^z \sigma_{0,c}^z \rangle$ and $\langle \tau^z \tau_{0,c}^z \rangle$ are nonzero on the Kondo destroyed side (denoted as σ KD and τ KD in Fig. 4(c)), and smoothly decrease as a function of the bosonic coupling across the QCP.

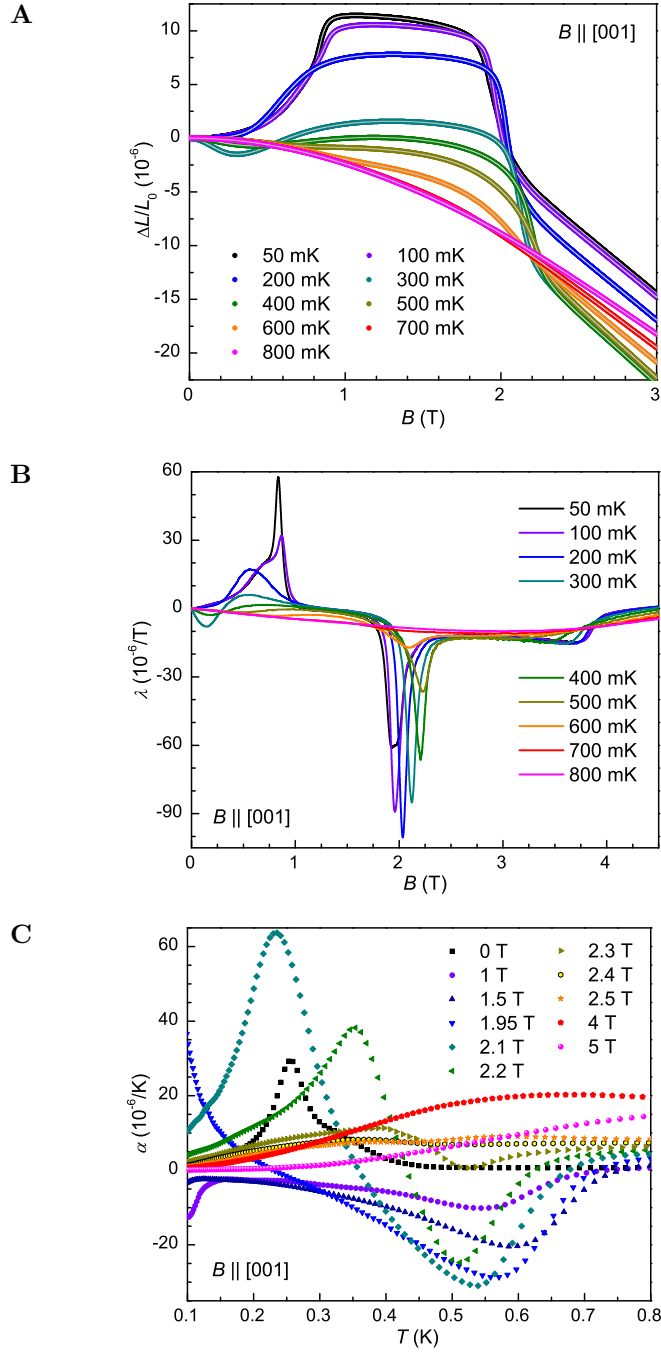


Fig. S1. Magnetostriction and thermal expansion of $\text{Ce}_3\text{Pd}_{20}\text{Si}_6$. (A) Relative length change $\Delta L/L_0$ along $[001]$ as function of magnetic field $B \parallel [001]$, at different fixed temperatures. The smooth variation of the length with field, down to the lowest temperature of 50 mK, confirms the second-order nature of the phase transitions at $B_N(T)$ and $B_Q(T)$. (B) Linear magnetostriction $\lambda = d(\Delta L/L_0)/dB$ vs. field isotherms, derived from the data in (A). The local maxima and minima in $\lambda(B)$ identify the magnetic fields at which a phase transition occurs for a given temperature (see symbols in Fig. 1(b)). (C) Temperature dependence of the linear thermal expansion $\alpha = d(\Delta L/L_0)/dT$ at different fields. The local maxima and minima in $\alpha(T)$ identify the phase transition temperature for a given magnetic field (see symbols in Fig. 1(b)).

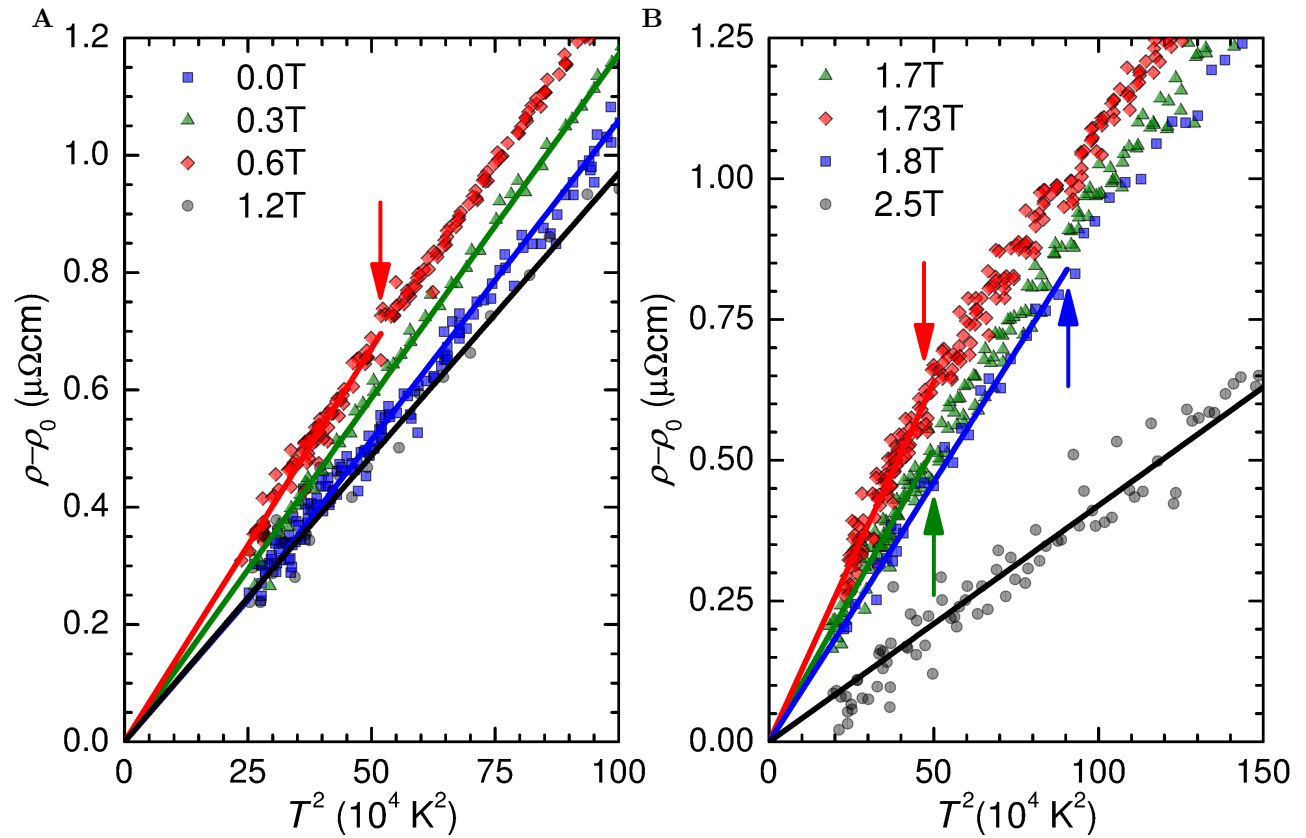


Fig. S2. Fermi liquid behavior of the electrical resistivity of $\text{Ce}_3\text{Pd}_{20}\text{Si}_6$ at the lowest temperatures. Electrical resistivity ρ minus its residual value ρ_0 vs. T^2 in the vicinity of the lower and upper quantum critical point in (A) and (B), respectively. The straight lines are best linear fits to the low-temperature data. They end at the temperatures where the fits deviate by more than 0.2% from the data (see arrows). The slopes of the fits correspond to the A coefficients shown in Fig. 2(d) of the main part.

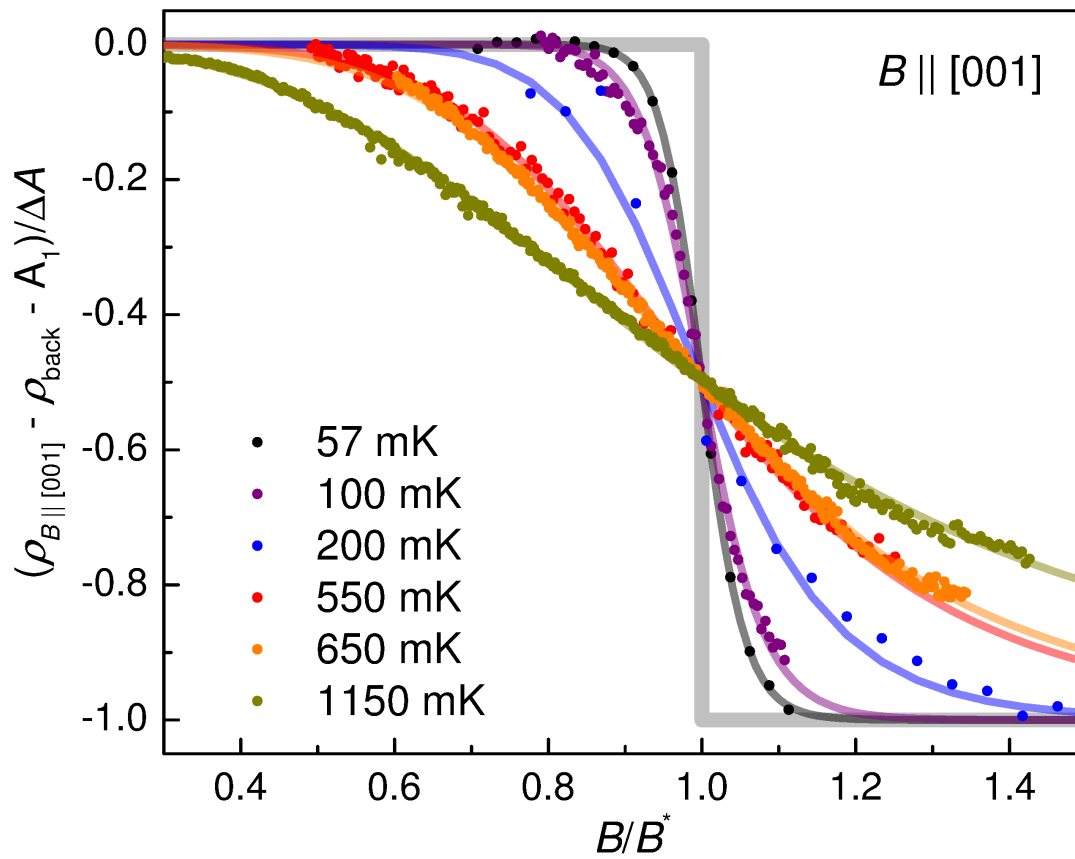


Fig. S3. Magnetoresistance crossovers of $\text{Ce}_3\text{Pd}_{20}\text{Si}_6$ in extended field range. Extended view of Fig.3(c) of the main part. Data for the different isotherms are shown in the field ranges where they obey the crossover behavior.

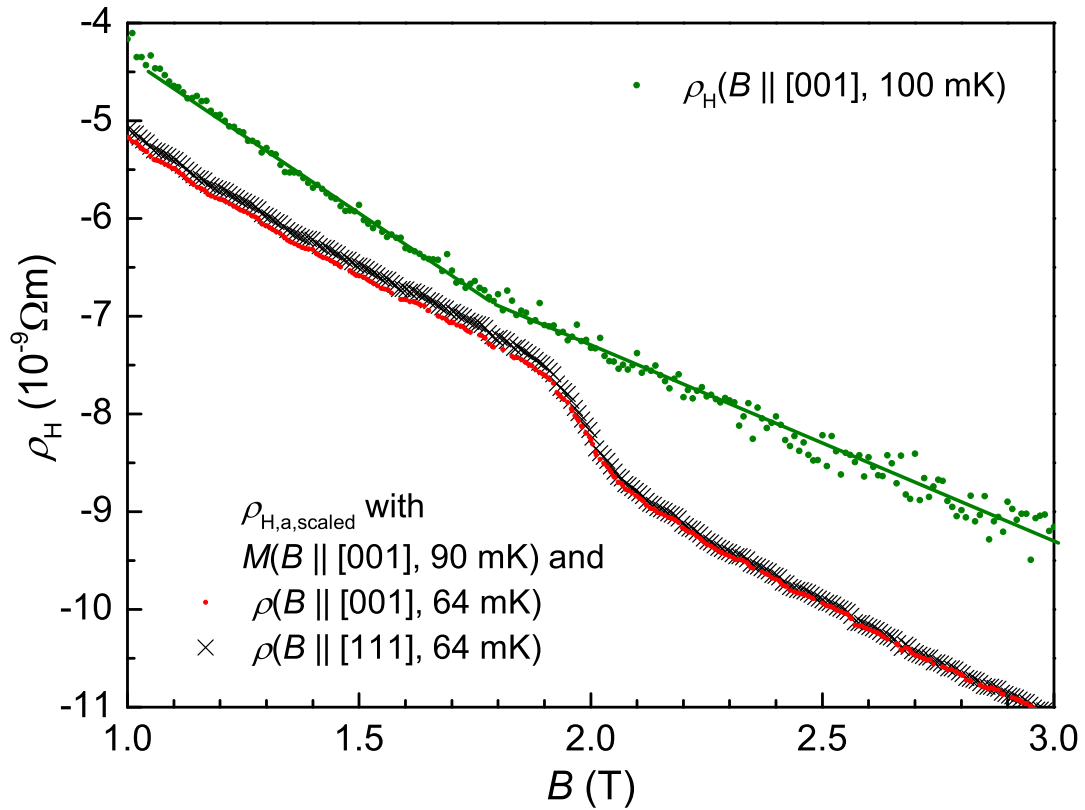


Fig. S4. Analysis of anomalous Hall effect. Measured Hall resistivity for $B||[001]$ at 100 mK (green dots, green lines are guides-to-the-eyes), together with hypothetical anomalous Hall contributions due to skew scattering (Section S3, Eqn. 3) determined from published magnetization data (3) and assuming that ρ_{skew} is either $\rho(B||[001])$ (red points) or $\rho(B||[111])$ (black crosses). $\gamma = 1.29 \times (-0.36) \text{ m}^2/\text{Vs}$ was used to bring $\rho_{\text{H}}^{\text{a}}$ to similar magnitude as the measured Hall resistivity ρ_{H} . The absence of a similar field dependence of $\rho_{\text{H}}^{\text{a}}$ and the measured ρ_{H} data rules out the importance of skew scattering in the vicinity of the quantum critical point at B_{Q} of $\text{Ce}_3\text{Pd}_{20}\text{Si}_6$.

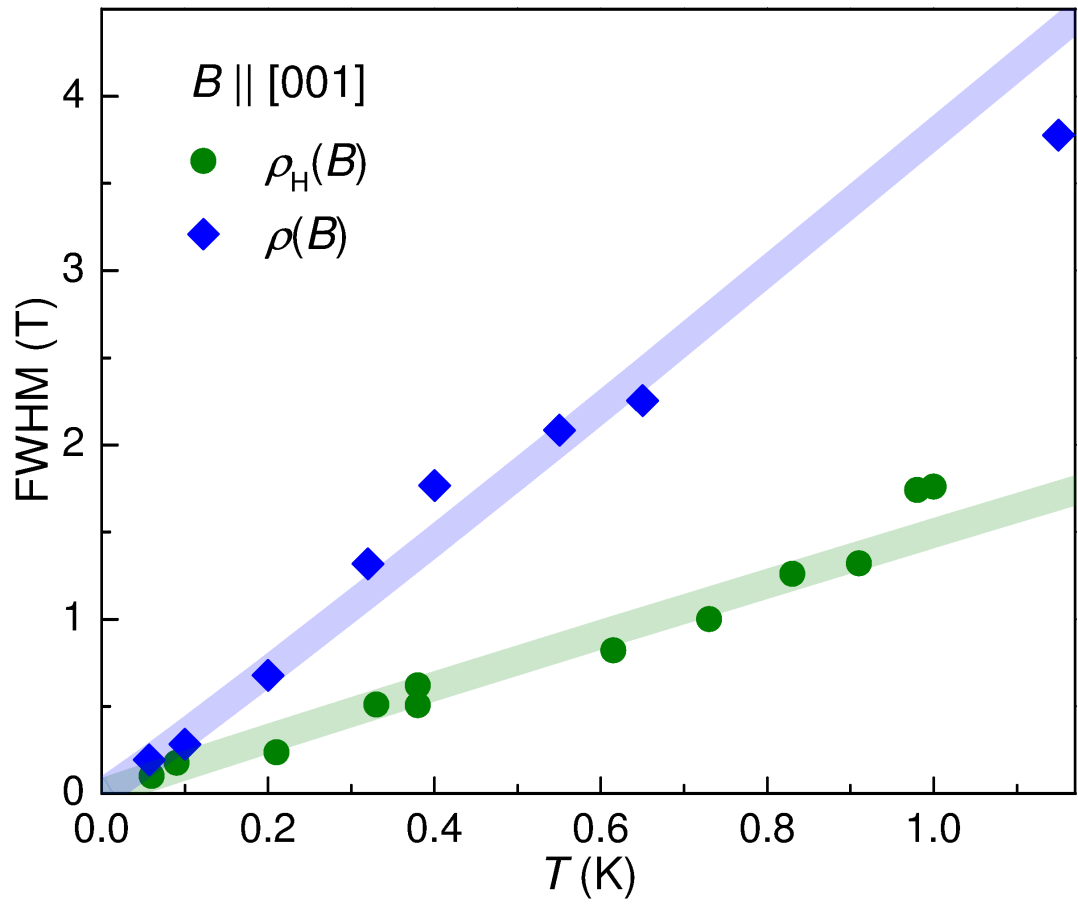


Fig. S5. Hall and resistivity crossover width on linear scales. Full width at half maximum of the crossovers in magnetoresistance and Hall resistivity derivatives of Fig. 3(g) of the main part, replotted on linear scales.

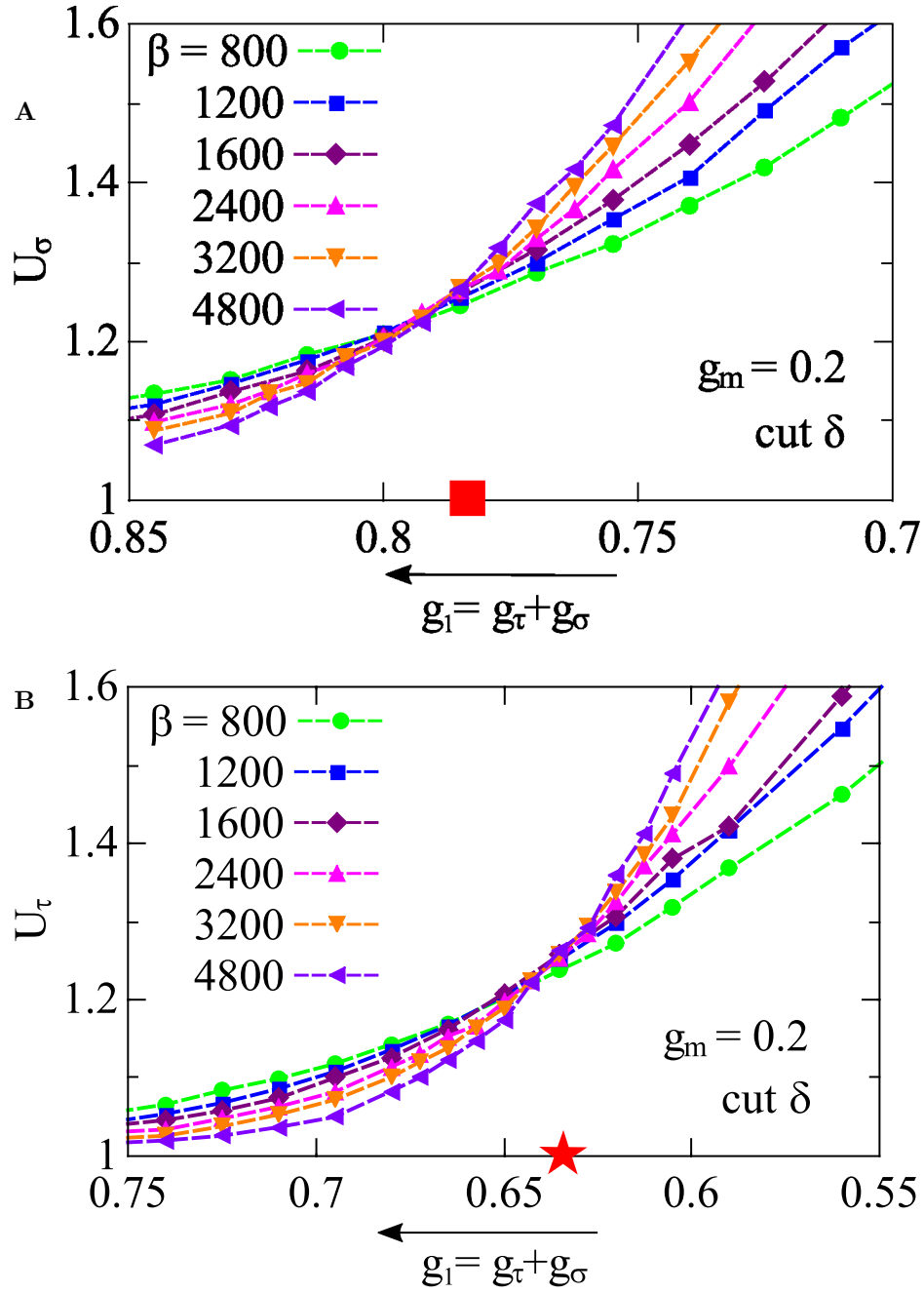


Fig. S6. Two consecutive QCPs in the multipolar Bose-Fermi Kondo model. Evolution of the Binder ratios U_σ for the spin (σ) channel in (A) and U_τ for the orbital (τ) channel in (B) (see Section S5 for the definition of U_σ and U_τ), as function of the coupling $g_1 = g_\sigma + g_\tau$ of spin and orbital degrees of freedom to the bosonic bath along cut δ in Fig. 4(b). The crossing points of U_σ and U_τ along this parameter cut (with each curve corresponding to a particular $\beta = 1/T$) marked by a red square and a red star in (A) and (B), respectively, demonstrate the presence of second-order quantum phase transitions.

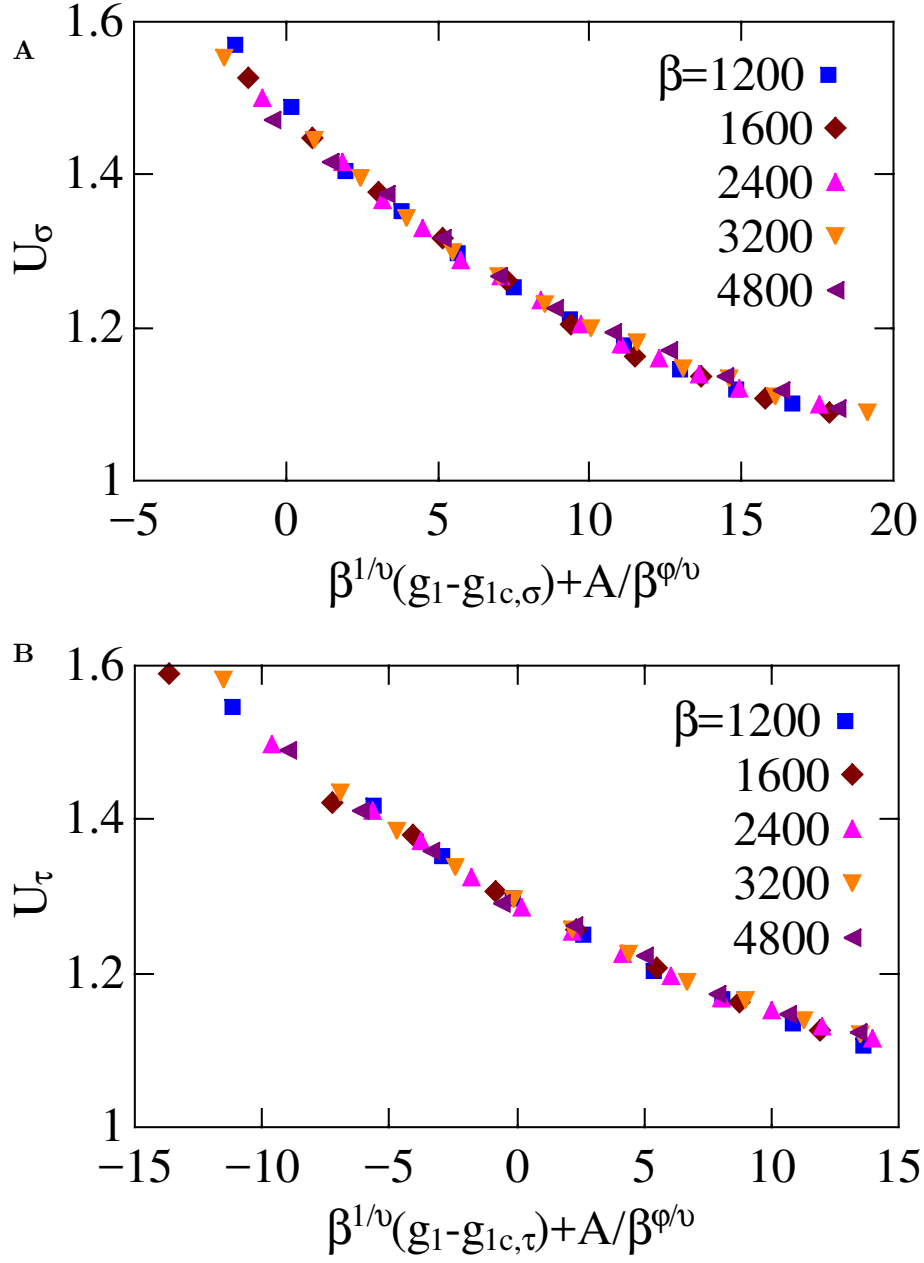


Fig. S7. Scaling plots of the Binder ratios. The collapse of the Binder ratios U_σ for the spin (σ) channel in (A) and U_τ for the orbital (τ) channel in (B) for different temperatures ($\beta = 1/T$) when plotted against $\beta^{1/\nu}(g_1 - g_{1c,\sigma}) + A/\beta^{\phi/\nu}$ and $\beta^{1/\nu}(g_1 - g_{1c,\tau}) + A/\beta^{\phi/\nu}$, respectively, evidences the presence of a quantum critical point (for the definition of U_σ , U_τ , ν , g_{c1} , A , and ϕ involved in the scaling analysis, see Section S5). The same cut as in Fig. S6 is taken. We find the critical value of the bosonic coupling at the QCP for the spin and orbital sector to be $g_{1c,\sigma} = 0.78$ and $g_{1c,\tau} = 0.64$, respectively. The reciprocal correlation length exponent is found to be $\nu^{-1} = 0.51$ for both QCPs.

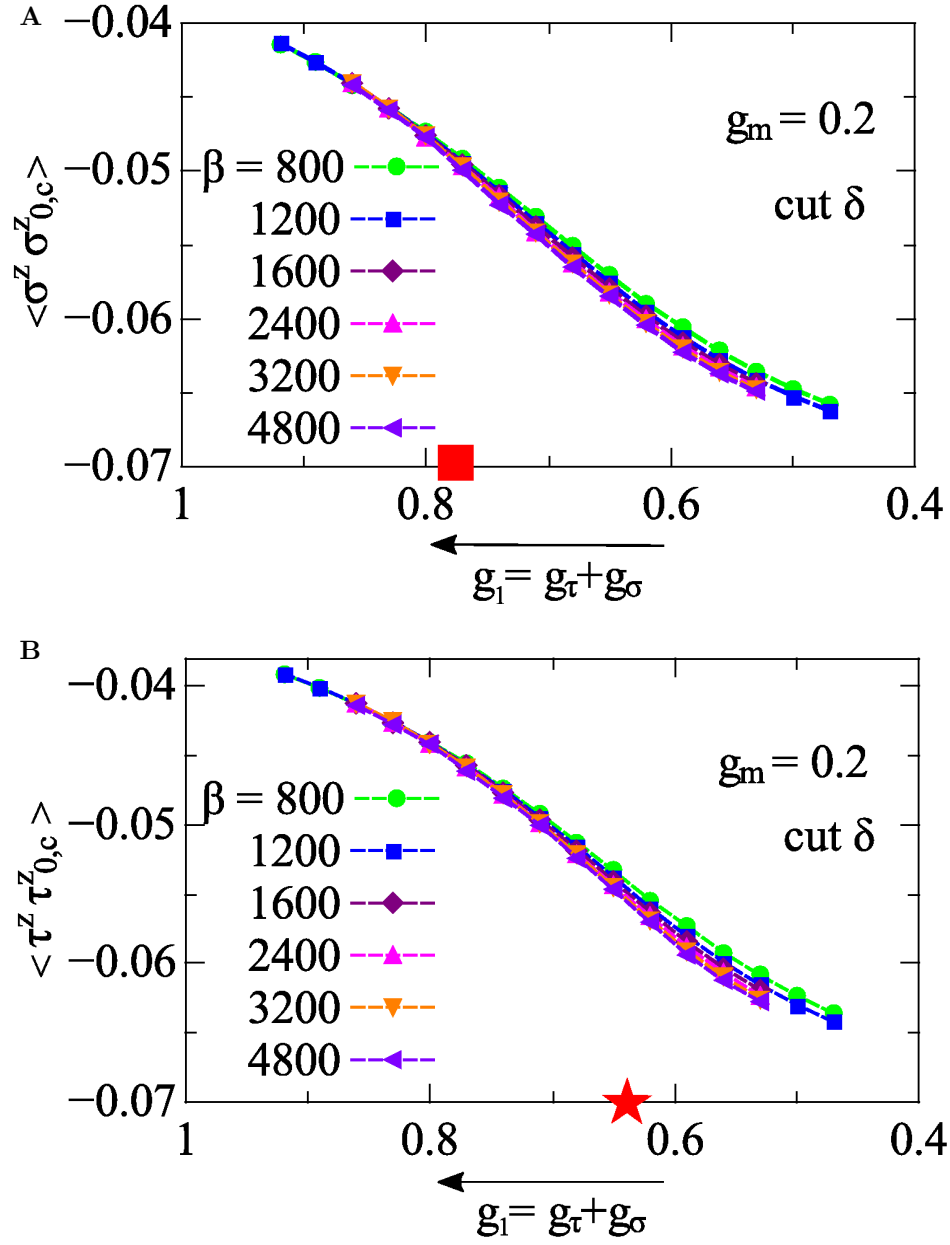


Fig. S8. Dynamical Kondo effect in the multipolar Bose-Fermi Kondo model. $\langle \sigma^z \sigma_{0,c}^z \rangle$ (A) and $\langle \tau^z \tau_{0,c}^z \rangle$ (B) vs bosonic coupling constant g_1 in the multipolar BFK model. The Kondo destruction QCPs in the spin and orbital sectors are marked with red square and red stars, respectively. Both quantities are nonzero in the fully Kondo destroyed and intermediate phases, thereby demonstrating the dynamical Kondo effect in each channel of Kondo destruction.

References

1. Prokofiev A, et al. (2009) Crystal growth and composition-property relationship of $\text{Ce}_3\text{Pd}_{20}\text{Si}_6$ single crystals. *Phys. Rev. B* 80:235107.
2. Ono H, et al. (2013) Magnetic phase diagram of clathrate compound $\text{Ce}_3\text{Pd}_{20}\text{Si}_6$ with quadrupolar ordering. *J. Phys.: Condens. Matter* 25(12):126003.
3. Mitamura H, et al. (2010) Low temperature magnetic properties of $\text{Ce}_3\text{Pd}_{20}\text{Si}_6$. *J. Phys. Soc. Jpn.* 79:074712.
4. Paschen S, et al. (2004) Hall-effect evolution across a heavy-fermion quantum critical point. *Nature* 432:881.
5. Custers J, et al. (2012) Destruction of the Kondo effect in the cubic heavy-fermion compound $\text{Ce}_3\text{Pd}_{20}\text{Si}_6$. *Nat. Mater.* 11:189.
6. Fert A, Levy PM (1987) Theory of the Hall effect in heavy-fermion compounds. *Phys. Rev. B* 36:1907.
7. Lorenzer KA (2012) Ph.D. thesis (Vienna University of Technology).
8. Portnichenko PY, et al. (2016) Incommensurate short-range multipolar order parameter of phase II in $\text{Ce}_3\text{Pd}_{20}\text{Si}_6$. *Phys. Rev. B* 94(24):245132.
9. Shiina R, Shiba H, Thalmeier P (1997) Magnetic-field effects on quadrupolar ordering in a Γ_8 -quartet system CeB_6 . *J. Phys. Soc. Jpn.* 66(6):1741.
10. Custers J, et al. (2012) Destruction of the Kondo effect in the cubic heavy-fermion compound $\text{Ce}_3\text{Pd}_{20}\text{Si}_6$. *SI of Nat. Mater.* 11:189.
11. Smith JL, Si Q (2000) Spatial correlations in dynamical mean-field theory. *Phys. Rev. B* 61(8):5184.
12. Chitra R, Kotliar G (2001) Effective-action approach to strongly correlated fermion systems. *Phys. Rev. B* 63(11):115110.
13. Hewson AC (1997) *The Kondo Problem to Heavy Fermions*. (Cambridge University Press, Cambridge).
14. Pang H (1994) Non-fermi-liquid states in a generalized two-channel kondo model. *Phys. Rev. Lett.* 73(20):2736–2739.
15. Le Hur K, Simon P, Borda L (2004) Maximized orbital and spin kondo effects in a single-electron transistor. *Phys. Rev. B* 69(4):045326.
16. Zhu L, Si Q (2002) Critical local-moment fluctuations in the bose-fermi kondo model. *Phys. Rev. B* 66(2):024426.
17. Zaránd G, Demler E (2002) Quantum phase transitions in the bose-fermi kondo model. *Phys. Rev. B* 66(2):024427.
18. Werner P, Millis AJ (2010) Dynamical screening in correlated electron materials. *Phys. Rev. Lett.* 104(14):146401.
19. Pixley JH, Kirchner S, Ingersent K, Si Q (2013) Quantum criticality in the pseudogap Bose-Fermi Anderson and Kondo models: Interplay between fermion- and boson-induced Kondo destruction. *Phys. Rev. B* 88(24):245111.
20. Binder K (1981) Finite size scaling analysis of Ising model block distribution functions. *Z. Phys. B* 43(2):119.
21. A. Cai, H. Hu, K. Ingersent, S. Paschen, and Q. Si (2019) Dynamical Kondo effect and Kondo destruction in effective models for quantum critical heavy fermion metals. *arXiv:1904.11471*.